Impact of secondary ice production on thunderstorm electrification under different aerosol conditions

Shiye Huang[1], Jing Yang[1,2,*], Qian Chen[1], Jiaojiao Li[1], Qilin Zhang[1], Fengxia Guo[1]

[1]Collaborative Innovation Center on Forecast and Evaluation of Meteorological Disasters (CIC-FEMD)/China Meteorological Administration Aerosol-Cloud and Precipitation Key Laboratory, Nanjing University of Information Science & Technology, Nanjing, 210044, China.
[2]China Meteorological Administration Key Laboratory of Cloud-Precipitation Physics and Weather Modification (CPML), Beijing, 100081, China.

Correspondence to: Jing Yang (jing.yang@nuist.edu.cn)

Abstract. Aerosol and secondary ice production (SIP) processes in convective clouds are both vital to charge separation in thunderstorms, but the relative importance of different SIP processes to cloud electrification under different aerosol conditions is not well understood. In this study, using the Weather Research and Forecasting (WRF) model with a spectral bin microphysics scheme, we investigate the role of four different SIP processes in charge separation in a squall line with different cloud condensation nuclei (CCN) concentrations, including the rime-splintering process, the ice-ice collisional breakup, shattering of freezing drops, and sublimational breakup. It is found that the simulation well reproduces the macro-morphology, the occurrence location, and the eastward tendency of the storm. As the CCN concentration increases, more but smaller cloud droplets can be lifted up to mixed-phase regions. The warm rain process is suppressed, and the declined raindrop concentration leads to fewer graupel particles. In a clean environment, the shattering of freezing drops is the most important SIP process to ice production at relatively warm temperatures, and the graupel concentration can be significantly enhanced. In a polluted environment, the rime-splintering process contributes the most to the graupel and ice production at relatively warm temperatures. The ice-ice collisional break-up process contributes the most to ice production at relatively cold temperatures. The noninductive charging rates exhibit a dipole structure with upper negative and lower positive regions. The implementation of four SIP processes as well as the increase in aerosol concentration both cause an enhancement of the noninductive charging rate. However, aerosol and SIP processes have opposite impacts on the charging reversal: higher aerosol concentration results in a colder reversal temperature, while SIP processes lower the reversal level. In a clean environment, the shattering of freezing drops process has the greatest effect on the noninductive charging rate, while in a polluted environment, both rime splintering and the shattering of freezing drops processes can have a significant effect. Without any SIP process, the increase in aerosols is not capable of modifying the charge structure. It is the rime-splintering process in a polluted environment responsible for the generation of a normal charge structure. Both the addition of the SIP processes and the increase in aerosol concentration favor the enhancement of the electric field.

1 Introduction

Thunderstorm, accompanied by lightning, is one of the most serious natural hazards to the public (Fierro et al., 2013). The charge structure of thunderstorms determines the frequency and intensity of lightning, and the charge separation within the clouds depends on the complicated dynamical and microphysical processes. The study of thunderstorms, especially their

35   microphysics and electrification, has been a hot topic in meteorology for decades (Takahashi, 1983; Saunders et al., 1991; Saunders and Peck, 1998; Mansell et al., 2005). However, the impact of different microphysical processes on cloud electrification is not fully understood. The uncertainty in modelling the microphysics leads to biased lightning prediction in numerical simulations. Among the various microphysical processes, aerosols and different ice crystal formation mechanisms play a crucial role (Pan et al., 2022; Phillips et al., 2020; Phillips and Patade, 2022; Yang et al., 2016; 2020).

40

Cloud condensation nuclei (CCN), which are aerosol particles capable of forming cloud droplets, play an important role in cloud microphysics. According to the Twomey effect, an increase in aerosol concentration leads to an increase in cloud droplet number concentration (Twomey, 1977). Due to water vapor competition, higher aerosol concentrations lead to smaller cloud sizes, causing smaller collision efficiencies. Collision coalescence is known as an essential process for warm-rain initiation.

45   This means that the increase in aerosol concentration suppresses the warm rain process, which is proven by observational studies. Satellite observations indicate the presence of non-precipitated supercooled liquid water near the cloud tops due to smoke over Indonesia (Rosenfeld, 1999) and urban pollution over Australia (Rosenfeld, 2000). In addition, sustained supercooled liquid water down to -37.5°C has been detected in continental mixed-phase clouds from aircraft measurements. (Rosenfeld and Woodley, 2000). These observational studies demonstrate that the increase in aerosol concentration reduces

50   cloud droplet size, which suppresses warm rain processes and favors the freezing of cloud droplets as well as facilitates hail growth and cold rain processes (Rosenfeld and Woodley, 2000; Rosenfeld et al., 2008). The aerosol impact on microphysics will eventually modify the electrification of thunderstorms (Pan et al., 2022).

The increase in aerosol concentration favors the presence of more small cloud droplets above the freezing level, which would

55   influence ice generation. In convective clouds, ice generation can be significantly enhanced by a variety of different secondary ice (SIP) processes (Hallett and Mossop, 1974; Korolev and Leisner, 2020; Mossop and Hallett, 1974; Phillips et al., 2017, 2018; Santachiara et al., 2014). Based on numerical simulations, Qu et al. (2020) found that the number concentration of ice splinters produced by drop-freezing fragmentation increases as low-level CCN concentration increases from 100 cm^{-3} to 1000 cm^{-3}, and decreases as CCN concentration increases from 1000 cm^{-3} to 2000 cm^{-3}. Mansell and Ziegler (2013) showed the ice

60   splinter production through the rime-splintering process increases remarkably CCN concentration increases from 700 cm^{-3} to 1500 cm^{-3}, and continues to increase until meeting a plateau above 3000 cm^{-3}. Tan et al. (2015) suggested that secondary ice produced by graupel collecting big cloud droplets (> 24 μm) under low CCN conditions is greater than that under high CCN conditions.

65 Since the SIP processes enhance ice production, they will inevitably affect the electrification in clouds with different CCN concentrations as collisional separation between ice crystals and graupel is the most important charging process (Mansell et al., 2005; Saunders et al., 1991; Saunders and Peck, 1998; Takahashi, 1978). Some previous studies have been conducted to investigate the impact of the rime-splintering process on electrification. Baker et al. (1995) find an inverted charge structure generated by rime splintering based on numerical simulations. Lighezzolo et al. (2010) extended the rime growth experiments

70 conducted by Hallett and Saunders (1979) and found the average charge of one ice splinter ejected from the graupel is -14 fC. Recently, studies of the impact of several other SIP processes on cloud electrification have appeared. Phillips and Patade (2022) investigated the impacts of three SIP processes on deep convection using the Aerosol–Cloud model, and they found the graupel–snow collisions account for the majority of the charge separated in the simulated storm, and the storm electrification can be significantly altered by SIP from ice-ice collisional breakup (Phillips et al., 2020; Phillips and Patade, 2022). Huang et

75 al. (2024) investigated the effects of three SIP mechanisms on cloud microphysics and electrification by a realistic simulation of a squall line and found that the SIP processes significantly affect the ice generation and charge separation. Without any SIP process, the storm had an inversed triple structure, while with all the SIP processes implemented, the storm obtained a normal dipolar charge structure. Yang et al. (2024) simulated a cold-season thunderstorm in southeast China using WRF model containing four SIP processes, the results suggested the rime-splintering process is the most important SIP process to cloud

80 electrification in their case.

Previous studies have demonstrated that both CCN and SIP processes are vital for thunderstorm electrification, but till now, to our best knowledge, no study has explored the relative importance of different SIP processes under different CCN concentrations in thunderstorms. Observation and simulation have merely confirmed the strong link between aerosols and

85 lightning activity through ice-phase particles but does not consider the various SIP processes (Chaudhuri and Middey, 2013; Khain et al., 2008; Lynn et al., 2020; Naccarato et al., 2003; Pinto et al., 2004; Shukla et al., 2022; Stallins et al., 2013; Tan et al., 2015; Wang et al., 2011). In this paper, the parametrizations of four SIP mechanisms, noninductive and inductive charging schemes as well as a bulk discharge model are implemented in WRF model with spectral bin microphysics scheme to simulate a squall line occurred in Southeast China on 29-30 May 2022. Sensitivity experiments are made using different CCN

90 concentrations and different mechanisms of SIP to study the impacts of SIP processes on cloud electrification under clean and polluted conditions. The SIP processes considered in this paper are rime splintering, ice–ice collisional breakup, shattering of freezing drops, and sublimational breakup of ice. The rest part of this work is structured as follows: Sect. 2 introduces the design for simulating the squall line. The results are displayed in Sect. 3. Sect.4 discusses and summarizes this study, respectively.

2 Case description and design of numerical experiments

2.1 Case description

The simulated mesoscale convective system (MCS) is a squall line that occurred at Southeast China from May 29th to May 30th, 2022 (unless otherwise noted, UTC time is used throughout the remainder of this paper). The geopotential height, temperature as well as wind field of 500 hPa and 850 hPa are shown in Figure 1. A deep trough occurred at 500 hPa and baroclinicity was present at 850 hPa (Fig. 1b and d). At 850 hPa (Fig. 1d), southwest winds prevailed at latitudes lower than 28°N, while northeast winds prevailed at latitudes higher than 28°N, suggesting the presence of low-level convergence. In addition, the humid conditions at low levels and the dry conditions at high levels (Fig. 1a and b) are suitable for the formation of convection.

Figure 3e illustrates the observed composite radar reflectivity of the squall line at 00:00, May 30th. The storm intensity could be demonstrated using radar reflectivity. The radar data used in this study are derived from the grid products provided by 32 S-band radars located across southeast China. Each radar has a detection radius of 230 km, a resolution of 250 m, and a 1°-beam-width. The radar takes 6 minutes to complete a volume scan containing 9 elevation angles (0.5, 1.5, 2.4, 3.4, 4.3, 6.0, 9.9,14.6, and 19.5°). As shown in the figure, this squall line was oriented southwest-northeast. The reflectivity in the strong convective core was approximately 55 dBZ. The storm moved towards the east with time, and dissipated after 06:00 UTC, May 30th (not shown).
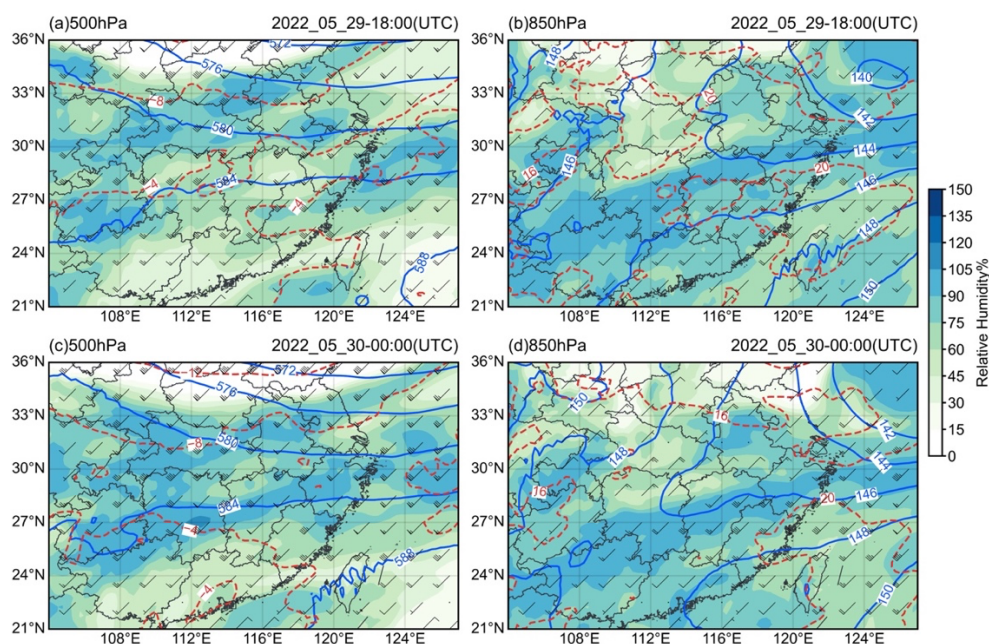

Figure 1. The Geopotential height (blue line), temperature (red line) and wind (black arrow) at 500hPa (a, c) and 850hPa (b, d). The shaded background represents relative humidity.

115

2.2 Description of model simulations

2.2.1 Cloud microphysics

The microphysics scheme used in two domains is the Fast-SBM scheme developed by Hebrew University Cloud Model (HUCM) (Khain et al., 2000). In contrast to the bulk microphysics scheme, this scheme uses 33 double mass bins to
120   characterize the particle size distribution. In previous studies, the effectiveness of the SBM and bulk schemes for simulating cloud microphysics is compared, and many studies suggested that the SBM scheme provides simulation results that are closer to real observations (Khain et al., 2009, 2015). In Fast-SBM scheme, the number concentration of CCN is calculated using an empirical formula (Pruppacher and Klett, 1997), the Twomey equation, $N_{CCN} = N_0 S_w{}^k$, where S_w refers to supersaturation with respect to water, N_0 represents the CCN concentrations at 1% supersaturation, and k is the slope of the CCN size
125   distribution. The default version of the fast-SBM scheme has different mechanisms of primary ice nucleation (Bigg, 1953; Meyers, 1992) but only a single SIP mechanism, which is the rime-splintering process (hereafter RS). In the present study, we implement three other mechanisms of SIP in the model: ice–ice collisional breakup (hereafter IC), shattering of freezing drops (hereafter SD), and sublimational breakup of ice (hereafter SK). The parameterization of the rime-splintering process is derived from two classical laboratory studies (Hallett and Mossop, 1974; Mossop and Hallett, 1974). Fragment production occurs
130   between -3°C and -8°C and reaches the maximum at -5°C. At -5°C, one ice fragment is generated for every 350 droplets collected by a graupel particle through the rime process. Phillips et al. (2017) has developed a theoretical formulation to describe secondary ice fragments produced during ice-ice collision based on an energy conservation principle and estimated theoretically uncertain parameters depended on laboratory and filed experiments (Takahashi et al., 1995; Vardiman, 1978). The production rate of ice splinters is related to particle size, rimed fraction, and temperature. More details could be found in
135   Phillips et al. (2017). Phillips et al. (2018) compiled previous laboratory studies and proposed a two-mode formulation to describe the fragmentation of freezing drops. The first mode of this fragmentation of freezing drops mechanism represents the collision between frozen drops and smaller ice particles and produces both big and tiny splinters. The second mode refers to the collision between frozen drops and bigger ice particles and produces tiny splinters. The first bin of Fast-SBM mass bins is used to represent the mass of tiny fragments. The number and size of ice splinters depend on parent drop size and environmental
140   temperature, as well as collision energy. More details can be found in Phillips et al. (2018). Deshmukh et al. (2022) proposed a formula to describe the number of ice fragments during sublimational breakup that applies only to dendritic ice crystals and heavily rimed particles (e.g., graupel). The size of parent ice particles and the relative humidity on ice control the number of ice fragments. More details can be found in Deshmukh et al. (2022).

2.2.2 Cloud electrification

It is known that the noninductive charge mechanism, referring to the rebounding collisions between graupel particles and ice crystals, is the primary charging mechanism in thunderstorms (Brooks et al., 1997; Mitzeva et al., 2006; Saunders et al., 1991; Saunders and Peck, 1998; Takahashi, 1978). The SP98 non-inductive charging parametrization (Saunders and Peck, 1998) based on the rime accretion rate (RAR) is implemented in this paper as in many previous studies (Fierro and Mansell, 2017; Fierro and Reisner, 2011; Huang et al., 2024; Yang et al., 2024). Besides, the inductive charging parameterization (Mansell et al., 2005) is also conducted in the SBM. Under the action of an electric field, the particles polarize through ions of opposite sign accumulating on opposite sides, and charge transfer may occur between particles when they collide and separate. A bulk discharge scheme is used in this paper, which can only simply release 30% charge at points where the electric field exceeds a threshold and cannot describe elaborate discharge channels (Fierro et al., 2013). Although more elaborate lightning models have been used in simulations, given the computational cost and the simple desire to relate the lightning rate to cloud microphysics properties, a bulk discharge scheme is used in this study.

The noninductive charging separation rate ($\frac{\partial \rho_{gi}}{\partial t}$) for two-colliding particle graupel and ice crystal is:

$$\frac{\partial \rho_{gi}}{\partial t} = \iint_0^\infty \frac{\pi}{4} \beta \delta q_{gi} (1 - E_{gi}) |\bar{V}_g - \bar{V}_i| (D_g + D_i)^2 n_g n_i dD_g dD_i \tag{1}$$

where, $|\bar{V}_g - \bar{V}_i|$ is the relative speed, D_g and D_i are the diameters, n_g and n_i are particle number concentrations, $E_{gi} = 0.01 \cdot \exp(0.1 \cdot T)$ is collection efficiency. β is used to control the charging process at low temperature:

$$\beta = \begin{cases} 1, & T > -30\,°C \\ 1 - \left[\frac{T+30}{13}\right]^2, & -43\,°C < T < -30\,°C \\ 0, & T < -43\,°C \end{cases} \tag{2}$$

Many parameterization schemes have been proposed to calculate δq_{gi}, which is the charge separated per rebounding collision. The parameterization scheme of δq_{gi} proposed by Saunders and Peck (1998) (hereafter SP98) is adopted in this paper. The formulation of δq_{gi} is:

$$\delta q_{gi} = B d^a V^b \delta q_\pm \tag{3}$$

where, $B, a,$ and b are constants related to crystal size (d), V is the relative fall speed. $\delta q_\pm$ is the separated charge in terms of riming accretion rate (RAR) and the critical RAR (RAR_C). For positive charging of graupel ($RAR > RAR_C$),

$$\delta q_+ = 6.74(RAR - RAR_C) \tag{4}$$

and for negative charging ($0.1\,gm^{-2}s^{-1} < RAR < RAR_C$),

$$\delta q_- = 3.9(RAR_C - 0.1)\left\{4\left[\frac{RAR - (RAR_C + 0.1)/2}{RAR_C - 0.1}\right]^2 - 1\right\} \tag{5}$$

RAR_C is a function of temperature. Therefore, aerosol and SIP processes not only affect the charging intensification, but also the sign of charge separation.

175   As shown in Mansell et al. (2005), the inductive charging rate is expressed as:

$$\frac{\partial \rho_g}{\partial t} = \left(\frac{\pi^3}{8}\right)\left(\frac{6.0\overline{V}_g}{\Gamma(4.5)}\right) E_{gc} E_r n_{t,c} n_{0g} D_c^2 \times [\pi\Gamma(3.5)\epsilon\langle\cos\theta\rangle E_z \mathcal{D}_{n,g}^2 - \Gamma(1.5)\frac{\rho_g}{3n_{t,g}}] \tag{6}$$

where $\Gamma(x)$ denotes the complete gamma function, E_{gc} and E_r represent the collision efficiency and the rebound probability, respectively. n_{0g} is the intercept of graupel number concentration, $\langle\cos\theta\rangle$ indicates the average cosine of the rebounding collision angle, E_z is the vertical electric field, ϵ is the permittivity of air, and ρ_g indicates the charge carried by graupel/hail.

180

2.2.3 Model setup

The real-case model of WRF is employed to simulate the squall line. The simulated domains are shown in Figure 2 and the resolution of these two nested domains are 9 km and 3 km, respectively. The number of the vertical level is 61 and the top pressure is 50 hPa for the two domains. The initial filed from 06:00 UTC on 29 May was established using FNL reanalysis

185   data with 0.25° × 0.25° resolution. The simulation starts at 06:00 UTC on 29 May 2022 and runs for 24 hours. The period lasting from 16:00 UTC on 29 May 2022 to 06:00 UTC on 30 May 2022 is of interest.
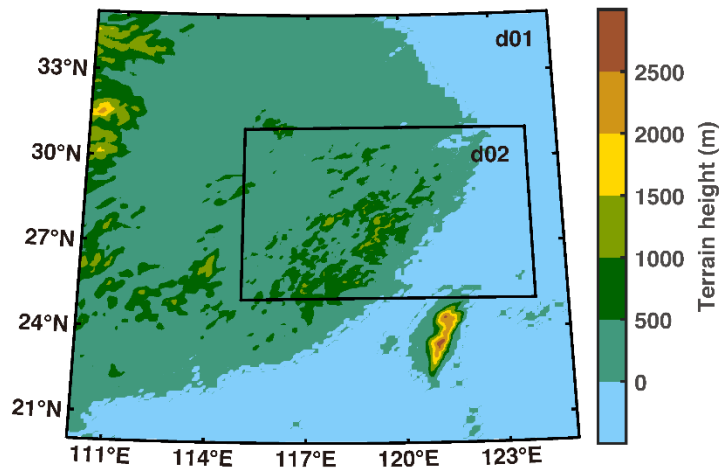

Figure 2. Terrain map of the model domain.

190   In the present study, the Kain-Fritsch cumulus scheme is activated in the outer domain while turned off in the inner domain. The shortwave and longwave are both parametrized using the Rapid Radiative Transfer Model (RRTM) (Mlawer et al., 1997). The Yonsei University planetary boundary layer scheme (Hong et al., 2006), the Revised MM5 surface layer scheme (Jiménez et al., 2012), and the Noah Land Surface Model (Tewari et al., 2004) are also employed in this paper.

195   In the present study, sensitivity experiments are conducted in two main aspects, on the one hand by activating different SIP processes and on the other hand by applying different CCN concentrations. To explore the significance of CCN concentrations for cloud microphysics and electrification, simulations are carried out with different settings of the coefficient N_0 in the Twomey equation: 400, 1000, 2000, and 4000 cm^{-3}. To investigate the impact of SIP, we conduct simulations with single or multiple SIP processes. The design of the sensitivity experiments is shown in Table 1. The first part of the experiment name

200   indicates activation of SIP: "noSIP" denotes that none of the SIP mechanisms is considered, "RS" means only rime splintering is implemented, "IC" means only ice-ice collision break up is used, "SD" means only shattering of freezing drops is used, "SK" means only sublimational breakup is considered, and "4SIP" means four SIP mechanisms are implemented in simulation. The number in each experiment name indicates the value of N_0.

205   **Table 1. Settings for 26 sensitivity experiments.**

Experiment	N_0	RS	IC	SD	SK
noSIP-400	400				
noSIP-1000	1000				
noSIP-2000	2000				
noSIP-4000	4000				
RS-400	400	×			
RS-1000	1000	×			
RS-2000	2000	×			
RS-4000	4000	×			
IC-400	400		×		
IC-1000	1000		×		
IC-2000	2000		×		
IC-4000	4000		×		
SD-400	400			×	
SD-1000	1000			×	
SD-2000	2000			×	
SD-4000	4000			×	
SK-400	400				×

SK-1000	1000				×
SK-2000	2000				×
SK-4000	4000				×
4SIP-400	400	×	×	×	×
4SIP-1000	1000	×	×	×	×
4SIP-2000	2000	×	×	×	×
4SIP-4000	4000	×	×	×	×

3 Results

3.1 Model validation

The radar reflectivity of four sensitivity experiments, noSIP-400, noSIP-4000, 4SIP-400 and 4SIP-4000, are shown and

210 compared with observations in Figure 3. Although the simulated radar reflectivity deviates to some extent from observations, the simulation results well reproduce the macro-morphology, the occurrence location, and the eastward tendency of this squall line. The addition of SIP processes and the concentration of aerosol particles have little effect on the macroscopic morphology of this squall line but had a significant effect on its intensity. The noSIP-400 experiment gives the strongest simulated radar reflectivity and significantly overestimates the observation (Fig. 3a). Considering four SIP processes provides simulated radar

215 reflectivity that is closer to observation than the noSIP experiments (Fig. 3c and d). The 4SIP-4000 experiment gives the closest results to observation (Fig. 3d). This squall line occurs in the coastal urban areas of China, where $N0=4000$ cm^{-3} seems more appropriate, as well as in the study by Qu et al. (2017).
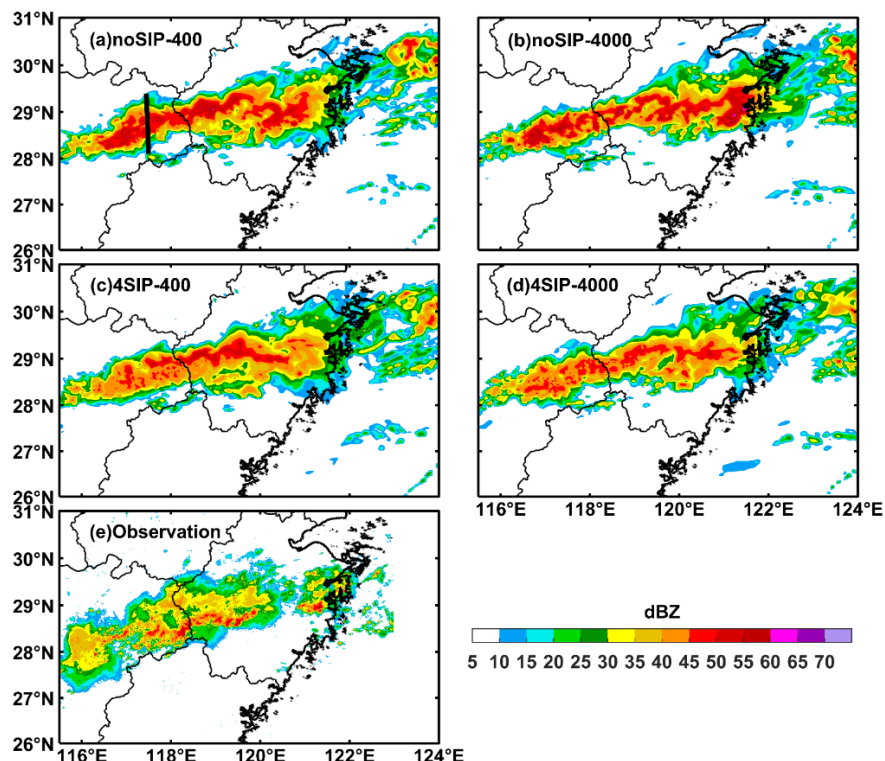
Figure 3. The observed and simulated radar reflectivity at 00:00, May 30th. The vertical black line in (a) shows the cross-section used in the subsequent investigation.

The contour-frequency-altitude figures (CFAD) of reflectivity are drawn to statistically analyze the differences between observed and modelled radar reflectivity at different altitudes (Figure 4). Overall, the modelled reflectivity is overestimated compared to the observation. The maximum reflectivity, which is found at melting level, occurs at about 5 km. The noSIP experiments yield the maximum reflectivity that are about 20 dBZ larger than the observed ones. With the implementation of four SIP processes, the maximum reflectivity decreases and is more consistent with the observation. As the CCN concentration increases, the maximum reflectivity becomes more biased from the observed value. It is noted that the radars may underestimate of the reflectivity at low levels due to the low-level beam being affected by ground clutter. In general, the fact that the radar reflectivity is reasonably well simulated and that the addition of the SIP processes improves the results gives us the confidence to study the effects of the SIP processes on cloud microphysics and electrification process under different aerosol conditions.
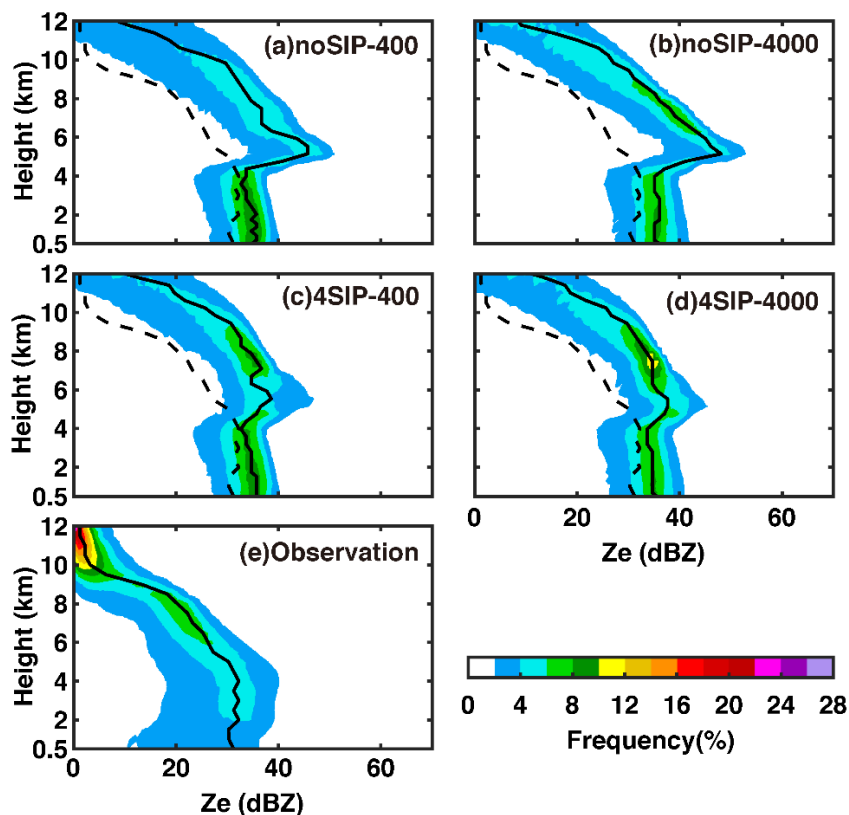
Figure 4. The CFAD of reflectivity between 00:00 and 04:00 on 30 May from (a) noSIP-400, (b) noSIP-4000, (c) 4SIP-400, (d) 4SIP-4000 and (e) observations. The black lines show the profiles of mean reflectivity, and the dashed lines in
235 **(a–d) are the observed mean reflectivity profiles.**

3.2 Impacts of SIP on cloud microphysics with different CCN concentrations

The impacts of aerosol and SIP processes on cloud microphysics in different sensitivity studies are analyzed in this section. Figure 5 shows the temporal evolution of the mixing ratios of graupel, ice/snow, rain, and cloud droplets for noSIP-400, noSIP-4000, 4SIP-400, and 4SIP-4000 experiments. The results are averaged over the cloud at different heights. As shown in the
240 figure, more CCN results in a higher cloud droplet mixing ratio (Fig. 5a-d). Regardless of SIP processes, the maximum mixing ratio of cloud droplets with N_0=4000 cm^{-3} is about 1.5 larger than that with N_0=400 cm^{-3}. Additionally, when N_0=4000 cm^{-3}, more cloud droplets could be lifted to higher altitudes, leading to more cloud droplets above the freezing level (Fig. 5a-d). In contrast, a higher concentration of CCN leads to a lower mixing ratio of raindrops (Fig. 5e-h) due to a less efficient warm rain process (Rosenfeld et al., 2008), and the graupel/hail mixing ratio is reduced as fewer raindrops are available for freezing (Fig.
245 5i-l). It is also noted that the ice/snow mixing ratio is slightly reduced by a higher CCN concentration, this is different from some previous studies which show more CCN can enhance ice concentration in convective clouds as more cloud droplets are available above the freezing level for freezing (Khain et al., 2008; Lynn et al., 2007). The reason is that the updraft strength is

weakened and the total water mixing ratio is reduced by higher CCN concentration in the present case, and will be discussed in more detail later in Figure 8.

250

The addition of SIP processes increases the mixing ratios of graupel/hail significantly (Fig. 5i-l). In the experiments with N_0=4000 cm^{-3}, the increase in the mixing ratio of graupel/hail induced by the SIP processes is greater than in a clean environment. In addition, the mixing ratio of ice/snow is also enhanced due to the addition of SIP processes (Fig. 5m-p), but the rainwater mixing ratio is not significantly affected (Fig. 5e and g). For N_0=4000 cm^{-3}, the addition of SIP processes results

255 in less liquid water mixing ratio above the freezing level (Fig. 5b, f, d, and h), probably due to the enhanced ice and graupel production and water depletion.
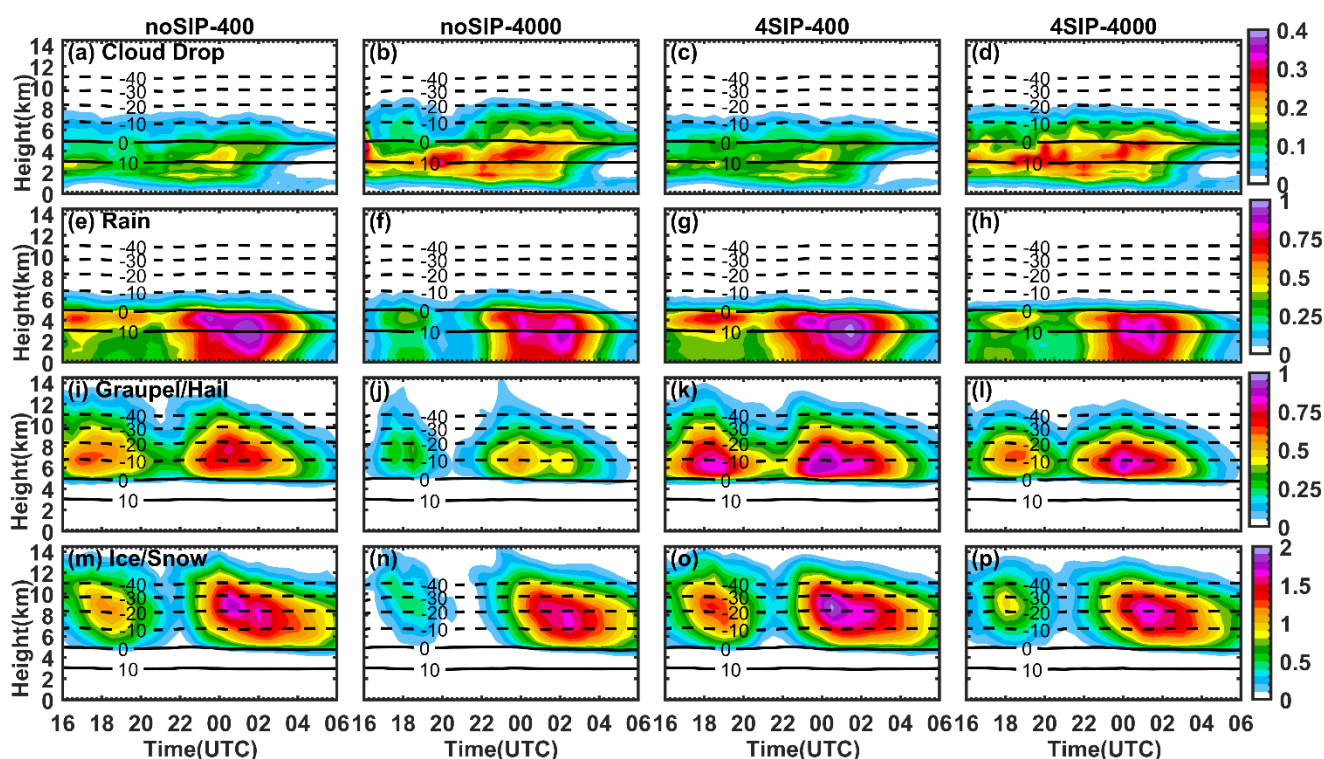
Figure 5. Time-height evolution of the mean mixing ratio (unit is g/kg) of four particles for four sensitivity experiments. (a-d) cloud drop, (e-h) rain, (i-l) graupel/hail, (m-p) ice/snow. The first to fourth columns represent the results from

260 **noSIP-400, noSIP-4000, 4SIP-400 and 4SIP-4000, respectively.**

The vertical profiles of mean number concentration and mean diameter of graupel/hail, snow/ice, rain, and cloud drops from noSIP-400, noSIP-4000, 4SIP-400, and 4SIP-4000 experiments are shown in Figure 6. As expected, more aerosols lead to a noticeable increase in the concentration of cloud droplets (Fig. 6a) but a substantial decrease in size (Fig. 6e). In addition, the

265 rain concentration significantly decreases in the experiments with N_0=4000 cm^{-3} (Fig. 6b). However, the raindrop size increases

as the CCN concentration increases (Fig. 6f). At temperatures warmer than -20°C, more aerosols lead to less but bigger graupel and snow particles without considering SIP processes (Fig. 6c and d).

The impacts of SIP processes are significant for graupel and snow while minor for liquid drops, this is found for experiments with different CCN concentrations. With the implementation of SIP processes, the graupel concentration increases significantly (Fig. 6c), while the graupel size decreases in the region warmer than -20 °C (Fig. 6g). The increases in snow concentration by SIP processes are mainly found at temperatures between 0 °C and -20 °C (Fig. 6d). Such increase is more profound for N_0=4000 cm^{-3}, resulting in a bimodal structure with an additional peak at -8 °C. This is because, for high concentrations of CCN, the RS process can significantly enhance ice production at relatively warm temperatures, while it is less efficient in a clean environment. We will demonstrate this statement later in Fig. 9.
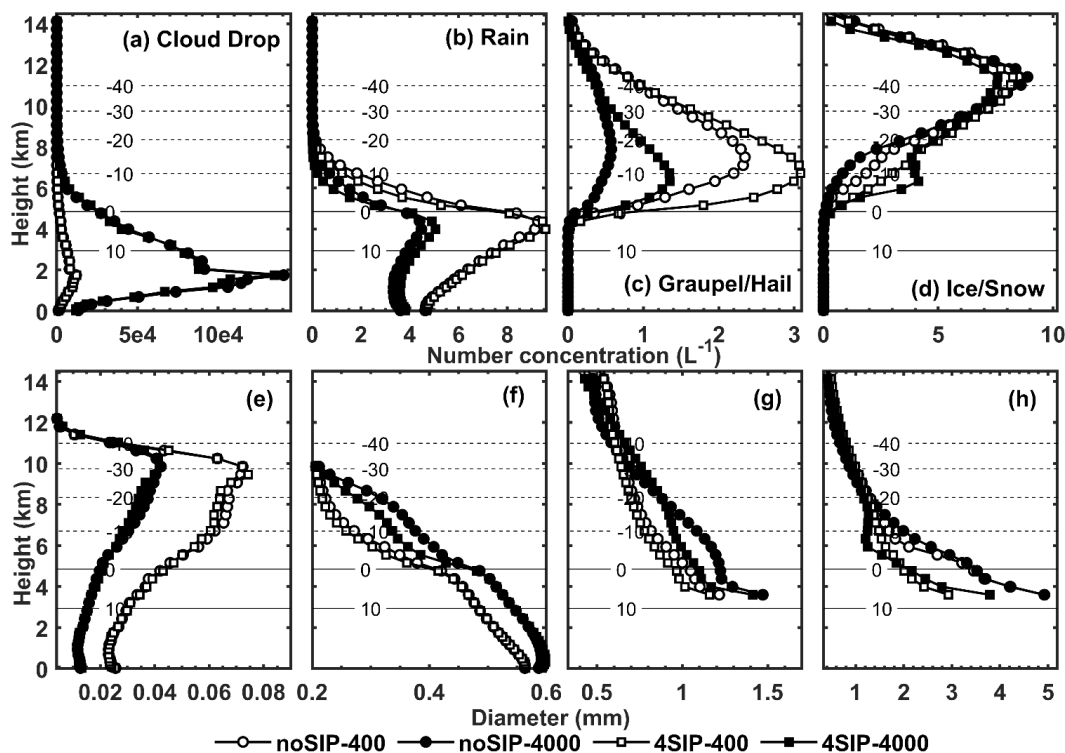

Figure 6. The vertical profiles of mean concentration (upper row) and mean diameter (lower row) of (a, e) cloud drop, (b, f) rain, (c, g) graupel/hail and (d, h) ice/snow from noSIP-400, noSIP-4000, 4SIP-400 and 4SIP-4000 experiment.

The average particle number concentrations and mixing ratios obtained from all the sensitivity experiments are summarized in Figure 7, which well illustrates the overall impacts of aerosol and SIP on cloud microphysics. In general, as N_0 increases from 400 cm^{-3} to 4000 cm^{-3}, the mixing ratio and number concentration of cloud droplets increase (Fig. 7a and b), while the mixing ratio and concentration of graupel and rain decrease (Fig. 7c-f). Although the number concentrations of ice/snow

particles vary imperceptibly among different sensitivity experiments, the mixing ratios of ice/snow particles in the noSIP
285   experiments are the largest (Fig. 7g). Interestingly, without any SIP process considered, the ice/snow mixing ratio and
concentration decrease as N_0 increases from 400 cm^{-3} to 1000 cm^{-3}, suggesting weakened ice nucleation. Although the cloud
droplet concentration is higher in noSIP-1000 than that in the noSIP-400 experiment, the droplets that can be lifted to upper
levels are insufficient to provide a higher ice concentration. In addition, the total water (liquid and ice) mixing ratio above the
freezing level is lower in the noSIP-1000 experiment than that in the noSIP-400 experiment. This finding implies an inhibited
290   convection by increasing CCN concentration, which is demonstrated in Figure 8. It is seen that the mean updraft strength is
relatively weak when N_0=1000 cm^{-3}, resulting in a lower total water mixing ratio. The decreased latent heat release due to less
drop freezing is the plausible explanation for the weakened updrafts as N_0 increases from 400 cm^{-3} to 1000 cm^{-3}. As N_0
increases from 1000 cm^{-3} to 4000 cm^{-3}, the updraft velocity varies non-monotonically with increasing aerosol concentration in
noSIP experiments, we do not see significant updraft enhancement and increase in total water mixing ratio, but the ice/snow
295   concentration is enhanced (Fig. 7h), suggesting the aerosols-impact on microphysics exceeds its impact on dynamics if the
CCN concentration is very high. We also investigated the maximum vertical velocity and obtained a similar conclusion (not
shown). However, the ice/snow mixing ratio is the lowest when N_0=4000 cm^{-3} though its concentration is high. This is because
more ice crystals compete for the limited water vapor and liquid water, leading to a lower ice growth rate. Some previous
studies also found this phenomenon in different case studies. Tan et al. (2015) noted that water vapor competition may result
300   in a decrease in the ice crystal mixing ratio at aerosol concentrations between 1000 and 3000 cm^{-3}. Qu et al. (2017) pointed
out that fewer snow crystals form in the simulation with more aerosols due to the declined depositional growth.
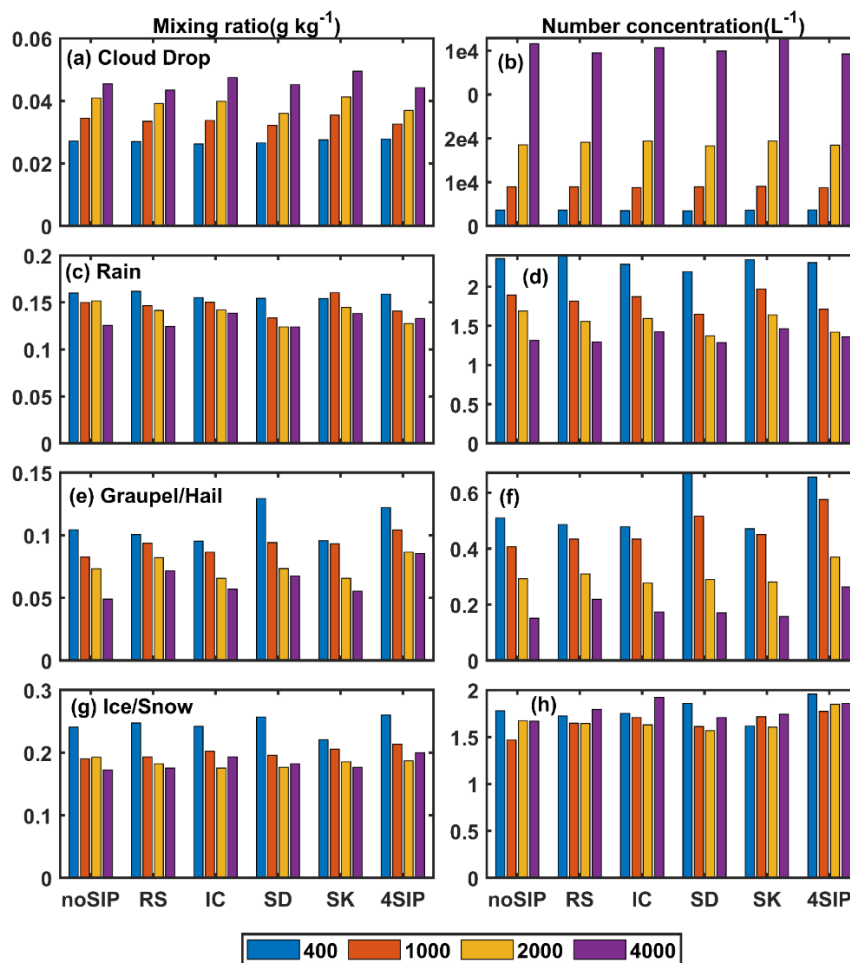
14

Figure 7. The time-domain-averaged mixing ratios (a, c, e, g) and number concentrations (b, d, f, h) of (a, b) cloud drop, (c, d) rain, (e, f) graupel/hail and (g, h) ice/snow from 26 sensitivity experiments.
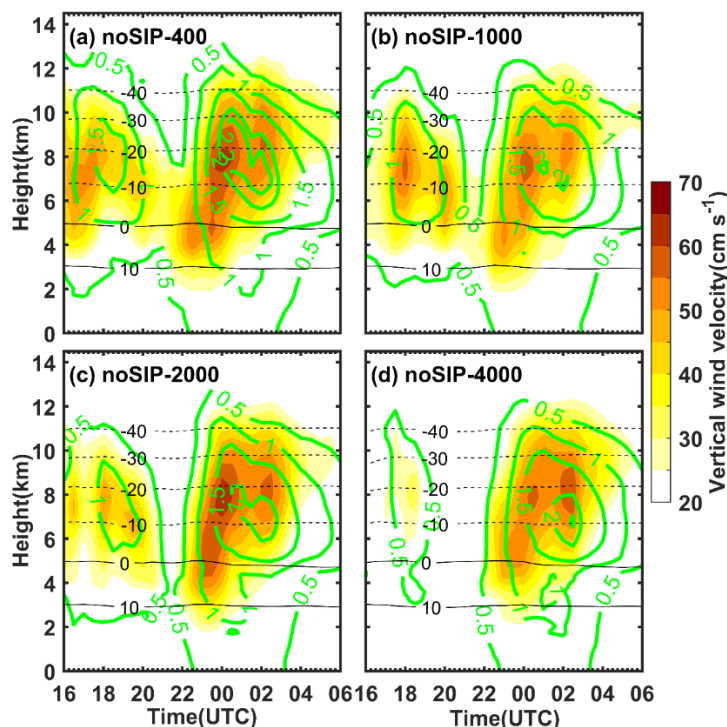
305

Figure 8．Time-height revolution of mean vertical wind velocity (cm/s, shaded) of (a) noSIP-400, (b)noSIP-1000, (c)noSIP-2000, (d)noSIP-4000. Green contour lines show all hydrometeors mixing ratio of 0.5, 1.0, 1.5, 2.0 and 2.2 g/kg.

310   Another important phenomenon found in Figure 7 is that the relative importance of the four SIP processes varies with different CCN concentrations. This can be better illustrated by combining Fig. 7 with the production rate of secondary ice (Figure 9). According to Fig. 9, it is clear that in a clean environment, SD produces the most secondary ice between 0 °C and -20 °C (Fig. 9i), and IC produces the most secondary ice between -10 °C and -20 °C (Fig. 9e). While in a polluted environment, the RS process has the highest secondary ice production rate between 0 °C and -10 °C (Fig. 9d). The SIP processes influence both the

315   graupel and ice concentrations. For graupel, SD is the most important SIP mechanism when N_0=400 cm^{-3} (Fig. 7f, blue bars) and N_0=1000 cm^{-3} (red bars), while as N_0 increases to 4000 cm^{-3}, the RS process contributes the most to the enhancement of graupel concentration (purple bars). This is consistent with Fig. 9, which shows the ice production rate through the RS process increases with increasing CCN concentration (Fig. 9a-d), while the SD is less significant when N_0=4000 cm^{-3} compared to N_0=400 cm^{-3} and N_0=1000 cm^{-3} (Fig. 9i-l). The IC process seems to have a strong enhancing effect on ice concentration,

320   especially for N_0=4000 cm^{-3} (Fig. 7h, purple bars), but it is efficient at relatively cold temperatures (between -10°C and -30 °C, Fig. 9e-h), and it has minor impacts on the graupel regardless of different values of N_0 (Fig. 7f). The size of secondary ice particles produced through IC are small, so the mixing ratio of ice is not significantly enhanced (Fig. 7g). The ice production rate through IC process decreases as N_0 increases from 400 cm^{-3} to 2000 cm^{-3}, and increases as N_0 increases from 2000 cm^{-3}

to 4000 cm^{-3} (Fig. 9e-h). This explains the variation of ice concentration in the experiments with only IC turned on (Fig. 7h).
But note that the results in Fig. 9 are from the experiments with all four SIP processes turned on, the other three SIP processes would also impact the cloud microphysics. One of the impacts is that the RS and SD process can enhance cloud glaciation at relatively warm temperatures, thus, fewer cloud droplets can be lifted to upper levels for freezing (Yang et al., 2024). This explains why the ice production rate through IC is lower for N_0=4000 cm^{-3} than N_0=400 cm^{-3} in Fig. 9, but the ice concentration is the highest for N_0=4000 cm^{-3} when only IC is considered in the model (Fig. 7h). The SK process occurs between -10 °C and -20 °C, but its ice production rate is orders of magnitudes lower than the others (Fig. 9m-p), thus, it has minor impacts on the microphysics in the present case.
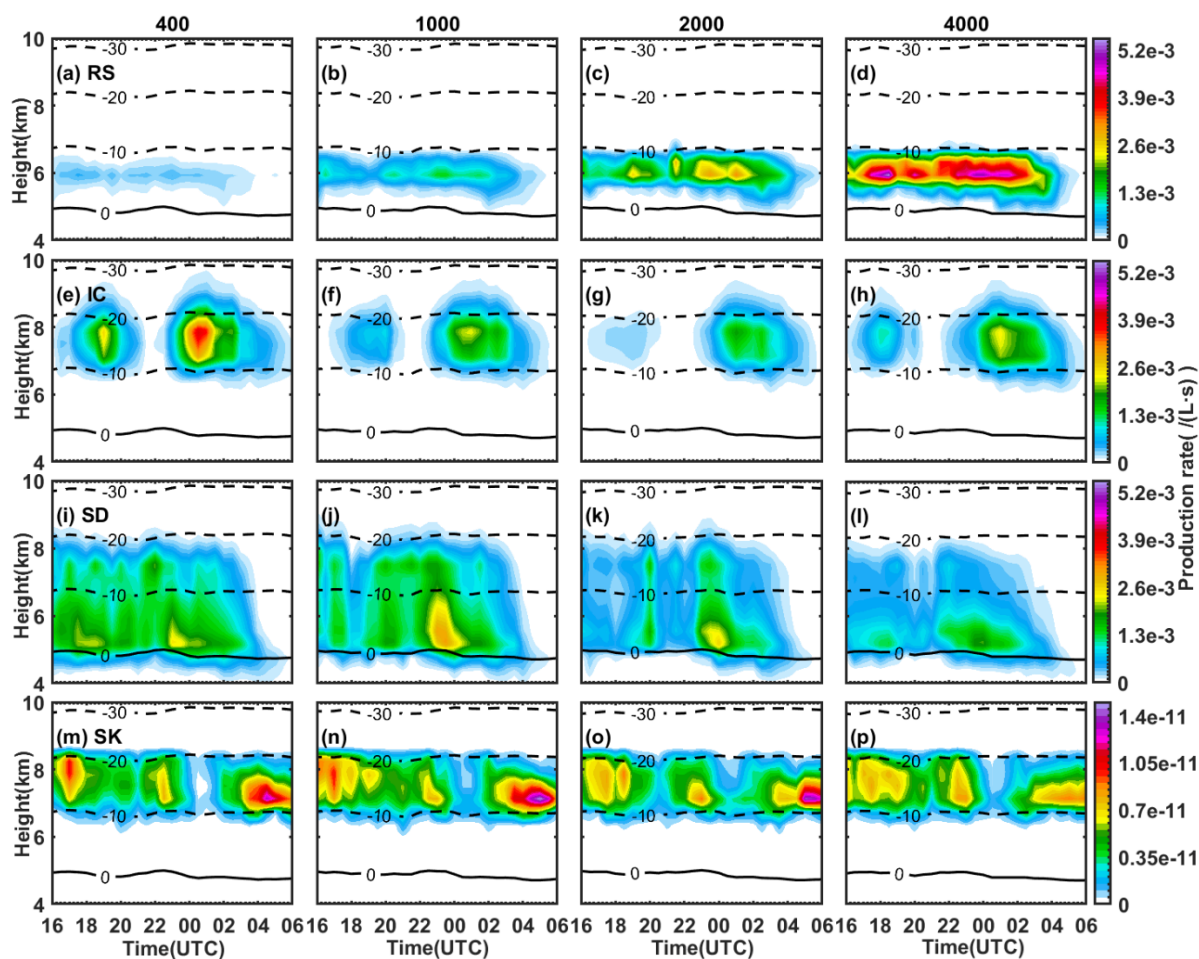
Figure 9. Time-height revolution of secondary ice production rate of four mechanisms of SIP. (a-d) rime-splintering process (RS); (e-h) ice-ice collisional breakup (IC); (i-l) freezing drop shattering (SD) and (m-p) sublimational breakup (SK). The first to fourth column indicate N_0=400, 1000, 2000, 4000 cm^{-3}, respectively.

To sum up, in the present case, the major impacts of aerosol and SIP processes on cloud microphysics are as follows, and we will show that they have substantial influences on cloud electrification.

1) More cloud droplets can be lifted to higher levels and the warm rain is suppressed as the CCN concentration increases.

340   2) Fewer graupel particles can form due to fewer rain-size drops for freezing as the CCN concentration increases.

3) Without any SIP process, the convective updraft is inhibited as N_0 increases from 400 cm^{-3} to 1000 cm^{-3}, leading to a lower total water mixing ratio and a lower ice concentration. However, the aerosol impact on ice microphysics exceeds its impact on dynamics as N_0 increases from 1000 cm^{-3} to 4000 cm^{-3}.

4) In a clean environment, SD is the most important SIP mechanism to ice production at relatively warm temperatures, and

345   the graupel concentration can be significantly enhanced.

5) In a polluted environment, RS contributes the most to the graupel and ice production at relatively warm temperatures. IC contributes the most to ice production at relatively cold temperatures.

3.3 Impacts of SIP on cloud electrification with different CCN concentration

350   Cloud electrification is associated with the collision between ice/snow and graupel and the interaction between droplets and graupel. Changes in cloud microphysics by aerosols and SIP processes can result in changes in thunderstorm charge structures. Figure 10 shows the temporal evolution of the noninductive and inductive charging rates. In general, the noninductive charging rate is significantly greater than the inductive charging rate, which is consistent with the opinion that the noninductive charging process is the main charging process of thunderstorms (Reynolds et al., 1957; Saunders et al., 1991; Takahashi, 1978, 1983).

355   The noninductive charging rate has a distinct dipole structure with upper negative and lower positive regions (Fig. 10a-d). Implementation of the four SIP processes as well as the increase in aerosol concentration causes an enhancement of the noninductive charging rate. It is noted that the reversal temperatures of noninductive charging rates are about -8℃ in the noSIP-400 experiment, -18℃ in the noSIP-4000 experiment, -5℃ in the 4SIP-400 experiment, and -15℃ in the 4SIP-4000 experiment, respectively (Fig. 10a-d), indicating aerosol and SIP processes have opposite impacts on the charging reversal:

360   higher CCN concentration results in a colder reversal temperature, while SIP processes lower the reversal level. The sign of the noninductive charging rate from the SP98 scheme depends on RAR, which is a function of liquid water content (LWC). In experiments with larger N_0, the reversal temperature position is elevated because more aerosols lead to more cloud droplets above the freezing level. The addition of four SIP processes enhances the ice concentration and leads to less LWC (Fig. 5 and 6), which consequently results in a warmer reversal temperature. The inductive charging rate is much smaller than the

365   noninductive charging rate, but it cannot be ignored. Similar to the noninductive charging rate, both the increase in CCN concentration and SIP processes can enhance the inductive charging rate (Fig. 10e-h). The inductive charging rate in the 4SIP-4000 experiment is the greatest among the four experiments. For 4SIP-400, the vertical electric field between 0℃ and -10℃ is positive, while the field between -10℃ and -20℃ is negative but very small (not shown). Graupel particles are negatively charged between 0℃ and -20℃ in 4SIP-4000 (Fig. 13l). Based on the Eq. 6 shown in section 2.2.2, it is suggested that the

370 performance of vertical electric field and graupel charge in 4SIP-4000 could result in an almost entirely positive induced

charging rate (Fig. 10h).
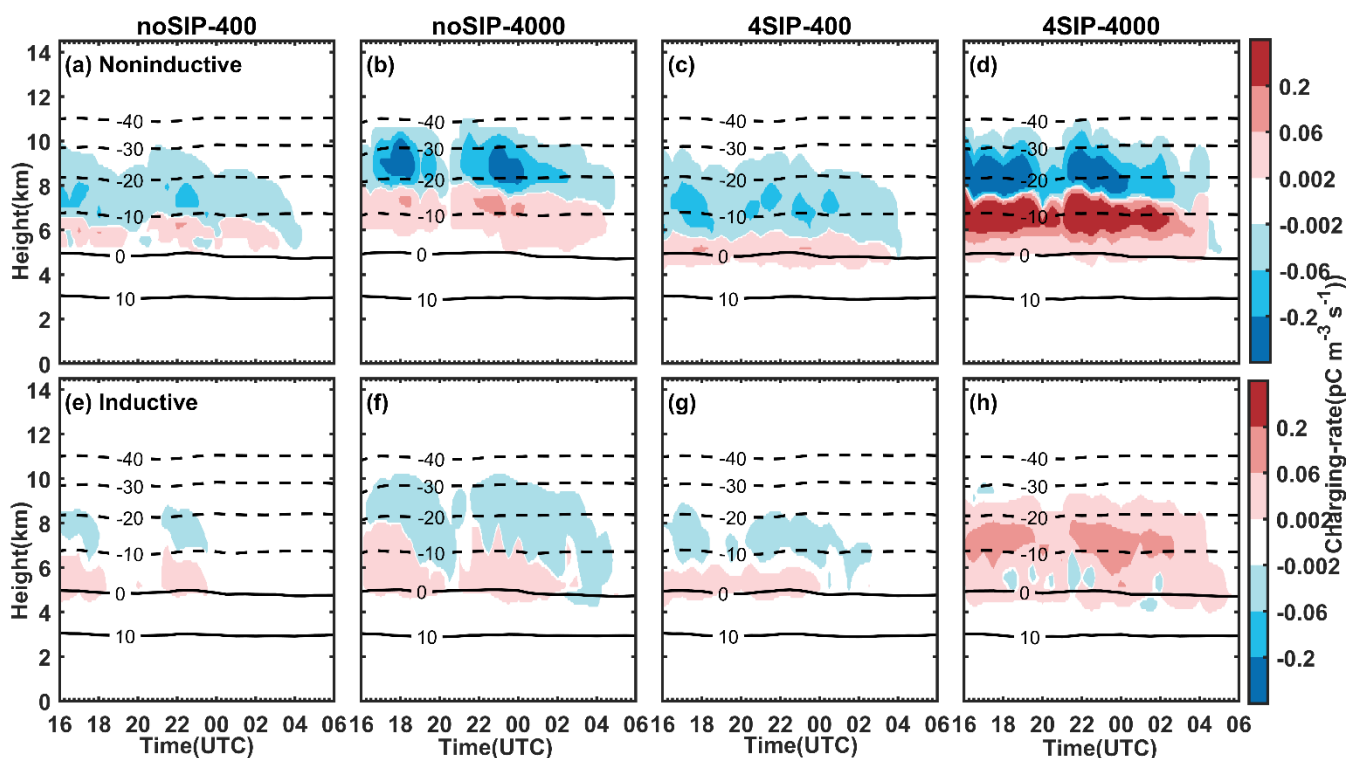
Figure 10. Time-height evolution of the mean charging rate (unit is pC/m³·s) for four sensitivity experiments. (a-d) noninductive charging rate, (e-h) inductive charging rate. The first to fourth columns represent the results from noSIP-
375 **400, noSIP-4000, 4SIP-400 and 4SIP-4000 experiment, respectively.**

The vertical profiles of the mean noninductive charging rate and mean inductive charging rate of the 26 sensitivity experiments are summarized in Figure 11. In all the experiments, the noninductive charging rate shows an upper negative and lower positive pattern (Fig. 11a-f). The magnitude of the noninductive charging rate increases as the CCN concentration increases. The IC
380 and SK process has a minor effect on the noninductive charging rate (Fig. 11c and e), as the IC process mainly affects the upper-level ice production, and the SK process is very weak in the present case. For $N_0=400$ cm^{-3}, the SD has the most significant impact on the noninductive charging rate. As N_0 increases to 4000 cm^{-3}, both the RS and SD process can result in a significant increase in the noninductive charging rate, in particular, the lower positive noninductive charging rate (Fig. 10b and d). With all four SIP processes considered and $N_0=4000$ cm^{-3}, the low-level positive noninductive charging rate is the
385 strongest among all the experiments (Fig. 11f). The magnitude of the inductive charging rate can be enhanced as the CCN concentration increases, but the structure remains similar (Fig. 11g). However, the RS and SD processes not only intensify the

19

inductive charging rate, but also significantly modify its vertical structure (Fig. 11h and j), and these two SIP processes dominate the vertical profiles of inductive charging rate in the experiments with all four SIP processes turned on (Fig. 11l).
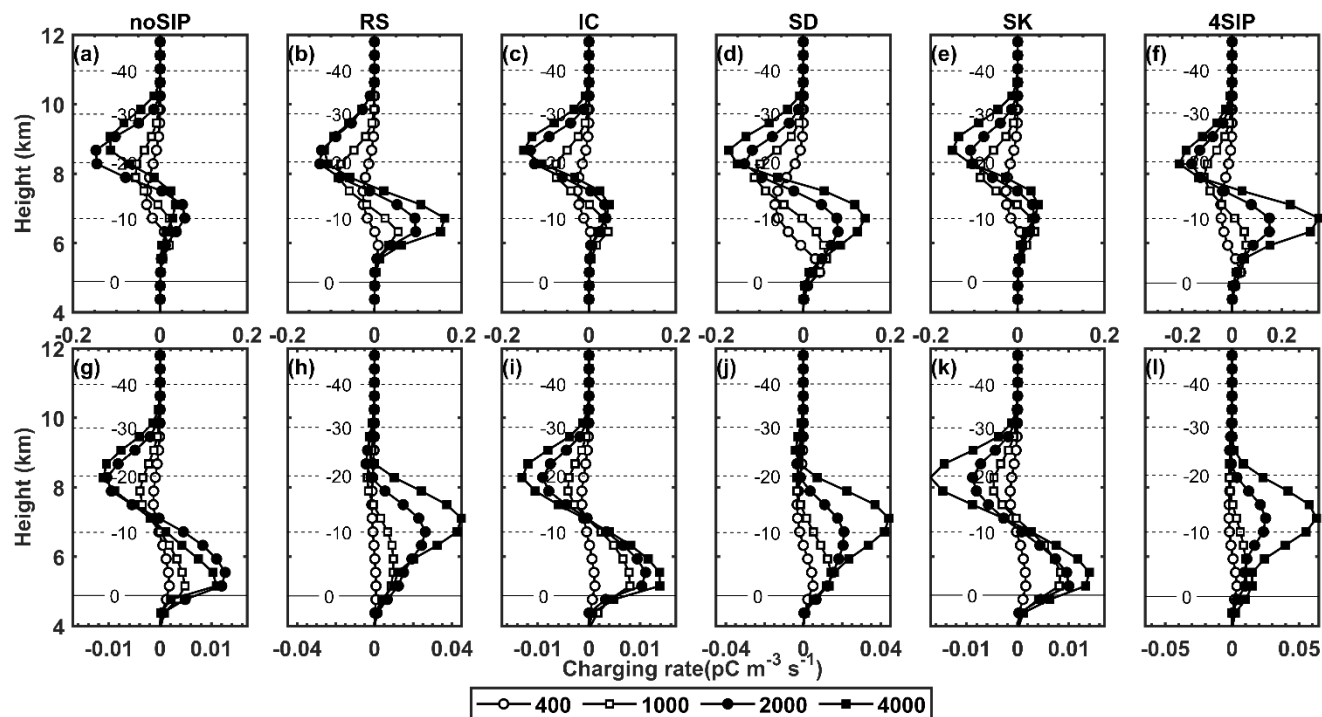

Figure 11. The vertical profiles of mean noninductive charging rate (upper row) and mean inductive charging rate (lower row). (a, g) noSIP, (b, h) RS, (c, i) IC, (d, j) SD, (e, k) SK and (f, l) 4SIP.

According to the analysis in Section 3.2, both ice and graupel concentrations and mixing ratios are lower in noSIP-1000 than in noSIP-400, so it is expected that the collision rate between graupel and ice would be weaker when N_0=1000 cm^{-3}, implying a negative effect on the noninductive charging. However, the modelled noninductive charging rate is greater in noSIP-1000 than in noSIP-400 (Fig. 11). The reason is the noninductive charging rate is not only a function of graupel-ice collision kernel, but also a function of RAR, which is related to the LWC. Figure 12 shows the RAR in the noSIP experiment under different aerosol concentrations. It is seen that the RAR increases with increasing CCN concentration, indicating it is the enhanced LWC carried by droplets above the freezing level dominates the aerosol impact on electrification. In addition, as the CCN concentration increases, RAR>0.1, which is the threshold of noninductive charging, extends to colder temperature regions. This is why a negative noninductive charging rate above the -30°C isotherm is present when N_0=4000 cm^{-3} (Fig. 11a).
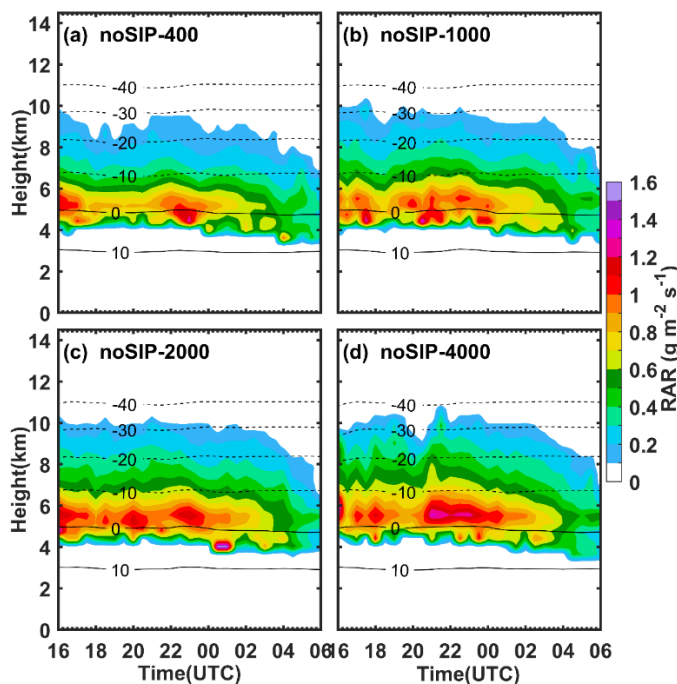
Figure 12．Time-height evolution of the mean RAR (unit is gm^{-2}s^{-1}) for four sensitivity experiments. (a) noSIP-400, (b)
405 **noSIP-1000, (c) noSIP-2000, (d) noSIP-4000.**

The significant impacts of aerosol and SIP on charging rate results in different structures of charge density in different experiments. Figure 13 shows the temporal evolution of charge density carried by graupel and ice/snow as well as the total charge density obtained from four sensitivity experiments. In the noSIP-400, noSIP-4000, and 4SIP-400 experiments, the

410 graupel particles have negative charge densities on average (Fig. 13a-c), this is related to the sedimentation of graupel. As illustrated in Fig. 10, in a clean environment, the negative charge carried by the upper-level graupel is considerably stronger than the positive charge carried by the lower ones. However, charging separation takes place at a relatively small area at a given time (Fig. 14), thus, the negative charge carried by the falling graupel may exceed the positive charge transferred to the graupel at low levels. The addition of SIP does not change the sign of charge density when the CCN concentration is low (Fig.

415 13c), but in the 4SIP-4000 experiment, a dipole structure is found (Fig. 13d). Due to the RS and SD processes, the positive charge transferred to the graupel through noninductive charging significantly increases below about -20℃, and exceeds the magnitude of upper-level negative charging (Fig. 10d). Therefore, graupel particles are on average negatively charged in the region colder than -20℃ and positively charged in the region warmer than -20℃ (Fig. 13d). The total charge density exhibits intensification as N_0 increases from 400 cm^{-3} to 4000 cm^{-3}. The addition of SIP processes also enhances the total charge density,

420 but in a clean environment, the storm remains an inverse triple structure, while in a polluted environment, the storm obtains a normal dipole structure.

21
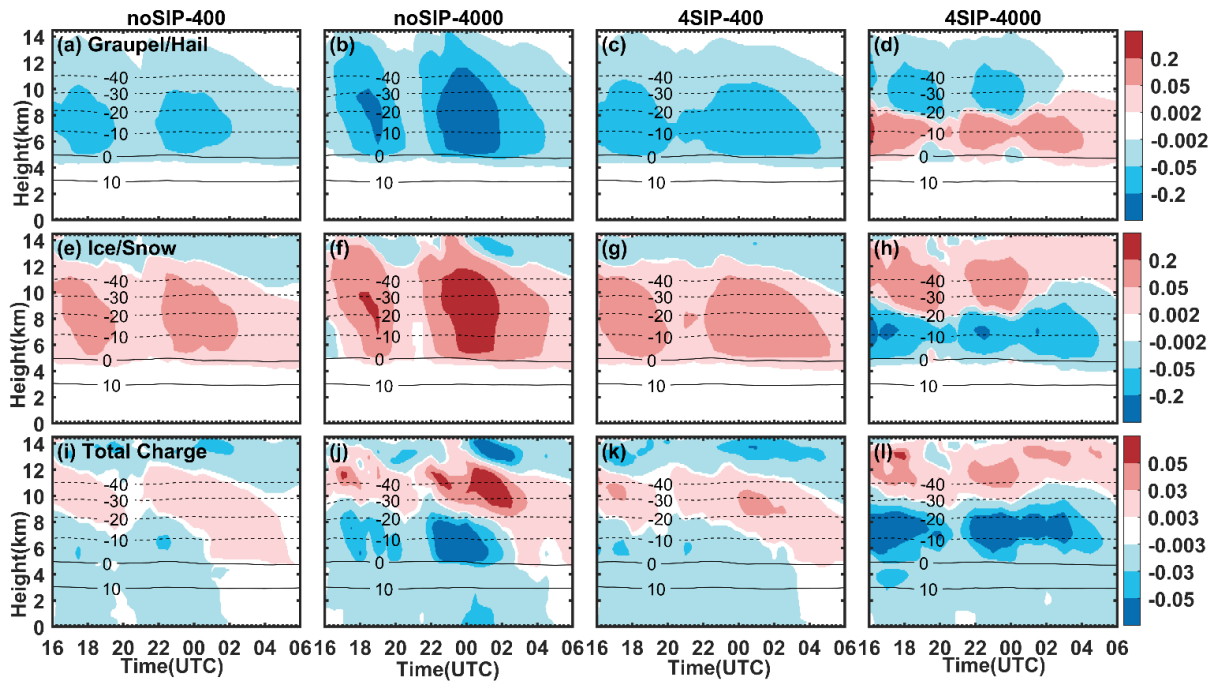
Figure 13. Time-height evolution of mean charge carried by graupel/hail (a-d) and ice/snow (e-h) particles as well as mean total space charge (i-l) (unit is $nC\ m^{-3}$) for four sensitivity experiments. The first to fourth columns represent the results from noSIP-400, noSIP-4000, 4SIP-400 and 4SIP-4000 experiment, respectively.
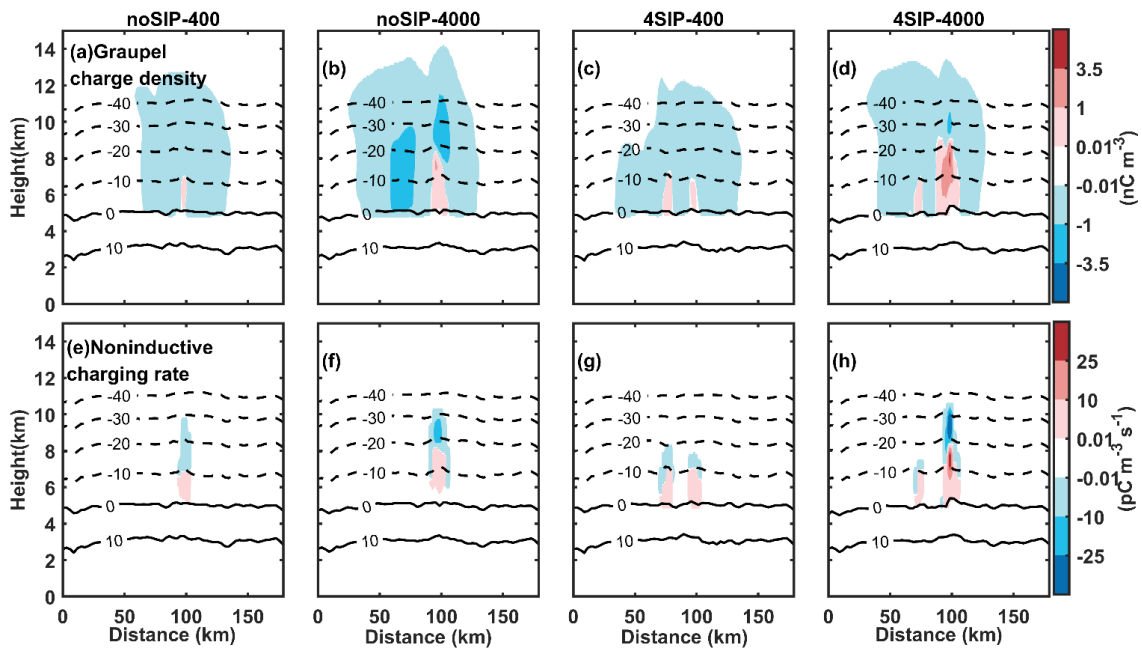

Figure 14. Cross sections of charge density and charging rate.

Since the RS and SD processes have greater impacts on cloud electrification in the present case, we investigate the average

430 vertical profiles of charge density from the sensitivity tests with the RS and SD processes implemented (Figure 15). It is seen that as N_0 increases from 400 cm^{-3} to 2000 cm^{-3}, the amount of charge carried by the graupel and ice/snow particles as well as the total charge increase markedly, while as N_0 increases from 2000 cm^{-3} to 4000 cm^{-3}, the charge carried by the graupel and ice/snow particles decreases, this is consistent with the modelled noninductive charging rate shown in Fig. 11a. When N_0 is 400 or 1000 cm^{-3}, the addition of RS has little effect on the amount and distribution of space charges, which is probably because

435 the cloud droplets are insufficient to induce a significant secondary ice production through the RS process. With the same N_0, the addition of SD enhances the amount of space charges, but it is not able to change the inverse triple structure of the total charge density. It is the RS process in a polluted environment responsible for the generation of normal charge structure. The combination of four different SIP processes can extend the positive charge region to higher levels.
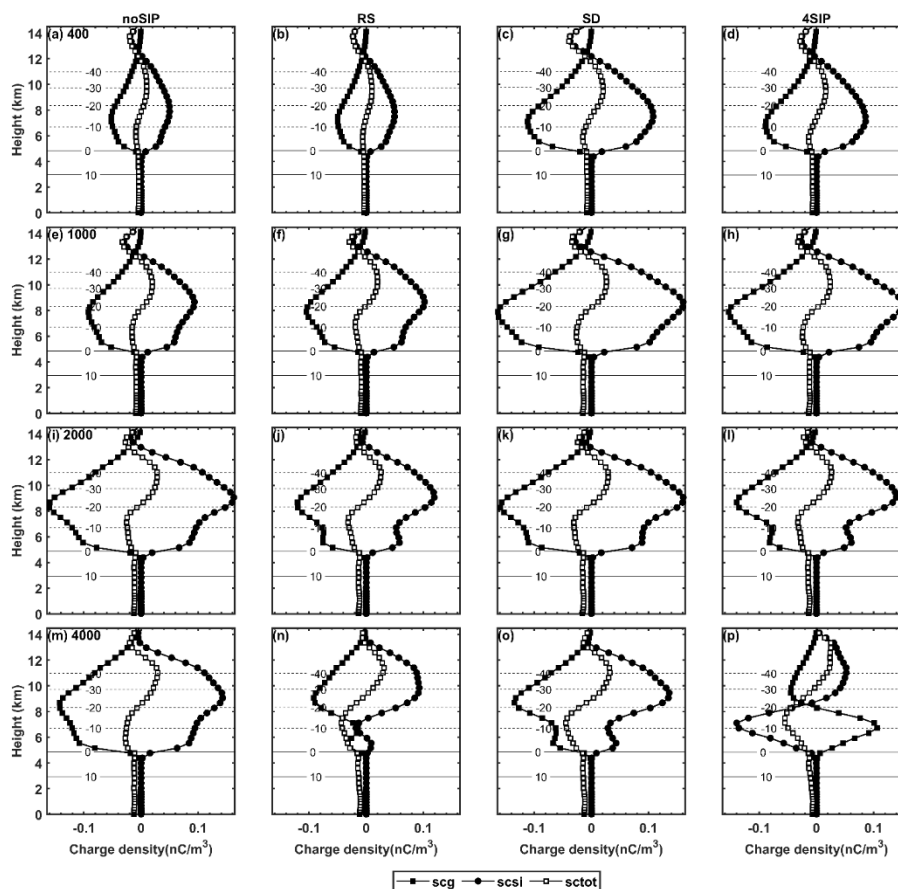

440 **Figure 15. The vertical profiles of mean charge carried by graupel/hail and ice/snow particles as well as mean total space charge for different sensitivity experiments. (a-d) N_0=400 cm^{-3}, (e-h) N_0=1000 cm^{-3}, (i-l) N_0=2000 cm^{-3}, (m-p)**

N_0=4000 cm^{-3}. The first to fourth columns represent the results from noSIP, RS, SD and 4SIP experiment, respectively. Black box lines represent graupel charge density, black dot lines represent ice/snow charge density and white box lines represent total charge density.

445

Modification of space charge density by aerosol and SIP processes would certainly influence the electric field. The time–height variations of the electric field obtained from four experiments are shown in Figure 16. The core of the maximum electric field is between 0℃ and -40 ℃, which coincides with the region where the charge is concentrated. Without any SIP process considered, the electric field after 22:00 UTC increase significantly as N_0 increases from 400 cm^{-3} to 4000 cm^{-3}, which is

450 consistent with the enhancement of total charge density shown in Fig.13. Considering four SIP processes, high CCN concentration cause remarkable increase in the electric filed between 0℃ and -30 ℃. It is clear the enhancement of the electric field is closely related to the enhancement of the total charge density. The comparison of electric fields obtained from the four experiments reveals that both the addition of the SIP processes and the increase in aerosol concentration favour the enhancement of the electric field.
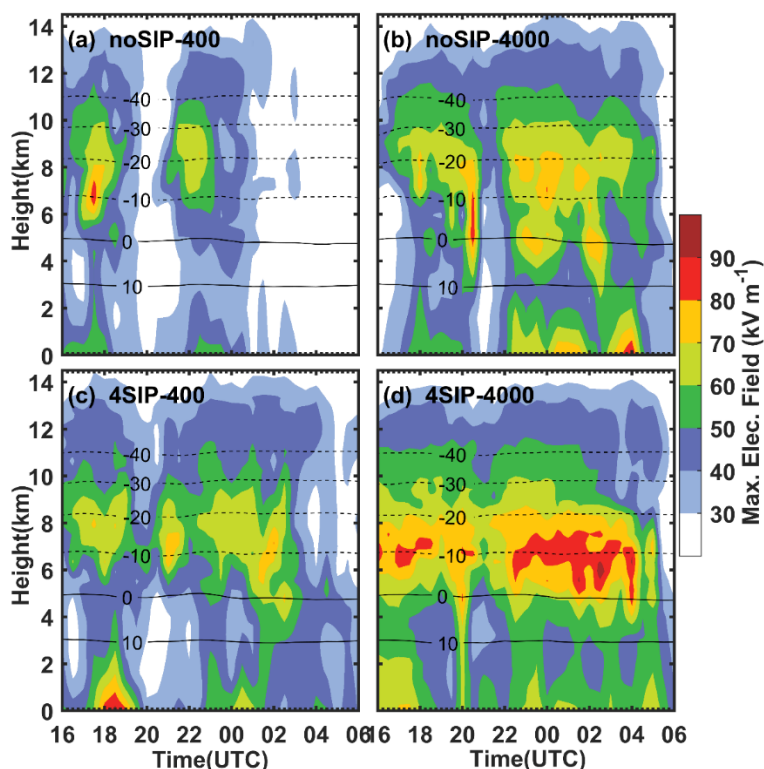
Figure 16. Time-height evolution of the maximum electric field for the noSIP-400, noSIP-4000, 4SIP-400 and 4SIP-4000 experiment.

455

4 Discussion and Conclusions

To investigate the effects of SIP processes and aerosols on cloud microphysics and electrification, the Fast-SBM microphysics
460   scheme with the addition of parameterizations of SIP, noninductive and inductive charging processes, and a bulk discharge
scheme are implemented to simulate a squall occurred on May 29-30, 2022, in southeast China. The results are concluded as
follows:

(1)   The simulation results well reproduce the macro-morphology, the occurrence location, and the eastward tendency of this
465   squall line. The addition of SIP processes and the concentration of aerosol particles have little effect on the macroscopic
morphology of this squall line but had a significant effect on its intensity. The 4SIP-4000 experiment gives the closest
results to observation.

(2)   Cloud microphysics characteristics are sensitive to SIP processes and aerosols concentration. More cloud droplets can be
470   lifted to higher levels and the warm rain is suppressed as the CCN concentration increases. Fewer graupel particles can
form due to fewer rain-size drops for freezing as the CCN concentration increases. Without any SIP process, the
convective updraft is inhibited as CCN concentration increases from 400 cm^{-3} to 1000 cm^{-3}, leading to a lower total water
mixing ratio and a lower ice concentration. However, the aerosol impact on ice microphysics exceeds its impact on
dynamics as CCN concentration increases from 1000 cm^{-3} to 4000 cm^{-3}. In a clean environment, SD is the most important
475   SIP mechanism to ice production at relatively warm temperatures, and the graupel concentration can be significantly
enhanced. In a polluted environment, RS contributes the most to the graupel and ice production at relatively warm
temperatures. IC contributes the most to ice production at relatively cold temperatures.

(3)   The noninductive charging rate is significantly greater than inductive charging rate. The noninductive charging rates
480   illustrate a distinct dipole structure having upper negative region and lower positive region. Note that implementation of
four SIP processes as well as the increase in aerosol concentration both cause an enhancement of the noninductive
charging rate. However, aerosol and SIP processes have opposite impacts on the charging reversal: higher CCN
concentration results in a colder reversal temperature, while SIP processes lower the reversal level. The IC and SK
processes have a minor effect on the noninductive charging rate. In a clean environment, the SD has the most significant
485   impact on the noninductive charging rate. In a polluted environment, both the RS and SD process can result in a significant
increase in the noninductive charging rate. The RS and SD processes not only intensify the inductive charging rate, but
also significantly modify its vertical structure.

(4)   In the noSIP-400, noSIP-4000 and 4SIP-400 experiments, the graupel particles have negative charge densities on average,
490   the ice/snow crystals are primarily positively charged as well as the total charge density demonstrates an inverse triple

25

structure, with a positive charge region sandwiched between two negative charges. In the 4SIP-4000 experiment, graupel particles are on average negatively charged in the region colder than -20°C and positively charged in the region warmer than -20°C and vice versa for ice/snow particles. In 4SIP-4000 experiment, total charge density exhibits a normal dipolar structure consisting of an upper positively charged region and a lower negatively charged region. Without any SIP process,

495   the increase in aerosols is not capable of modifying the charge structure. It is the RS process in a polluted environment responsible for the generation of the normal charge structure.

(5)   Both the addition of the SIP processes and the increase in aerosol concentration favor the enhancement of the electric field in the thunderstorm.

500

The results of this paper emphasize the necessity of adding SIP processes in the numerical model and importance of aerosol concentration for numerical simulations. Studying the effects of SIP processes and aerosol concentrations on cloud microphysics and electrification simultaneously is a new thinking of thunderstorm simulation.

505   In this paper four aerosol concentrations are considered. Many previous studies have shown that the effect of aerosols on cloud microphysics and electrification is not linear. Mansell and Ziegler (2013) set 13 values of aerosol concentration from 50 to 8000 cm^{-3} to investigate the effect of aerosols on storm electrification and precipitation. They found that graupel increased as the CCN concentration increased from 50 to 2000 cm^{-3}, but slowly decreased as the concentration increased above 2000 cm^{-3}. Additionally, Tan et al. (2015) designed simulation experiments with CCN concentration from 50 to 10000 cm^{-3}. It is found

510   that more cloud droplets, graupel and ice crystal production lead to a stronger charge separation with aerosol concentration varying from 50 to 1000 cm^{-3}. In contrast, the mixing ratio of ice crystal decreased in the aerosol concentration range of 1000-3000 cm^{-3}. Qu et al. (2020) not only studied the sensitivity of N_0 to SIP processes but also that of the shape parameters k in the Twomey formula and found that less ice splinters produced with larger k. The increase in k increases the smaller aerosol and decreases larger aerosol. As shown in this paper, more but smaller cloud droplets suppress warm rain process and have great

515   impact on the secondary ice production rate. Therefore, a wider range of N_0 and *k* maybe appropriate to explore the response of SIP processes to aerosols and obtain the optimal N_0 and *k* for producing the most ice splinters.

Tan et al. (2015) found that the charge structure remains constant as the aerosol increases. The results from Phillips and Patade (2022) indicated that the charge structures of the sensitivity experiments with different SIP processes and aerosol

520   concentrations are almost the same. Shi et al. (2019) found that the charge structure at different convective intensities became more complex as the aerosol increased. Compared to low aerosol concertation case, a notable inverted dipole charge structure was simulated in high aerosol concertation case (Sun et al., 2024). In this paper, with high aerosol concentrations, it is noted that the addition of four SIP processes could modify the total charge density from an inverted tripolar structure to a normal dipole structure, and apparently rime splintering and freezing droplet shattering processes play an incredibly important role in

525　this. The responses of different noninductive charging parameterizations to the combination of different SIP processes and different aerosol concentrations are also worth exploring in the future.

Data availability

The WRF model is available on https://www2.mmm.ucar.edu/wrf/users/download/get_source.html (NCAR MMM, 2023). The reanalysis data used to drive the WRF model, the observed radar reflectivity, sounding data, and lightning data are available
530　at https://doi.org/10.5281/zenodo.7968790 (Huang, 2023).

Author contributions

SH and JY implemented the parametrizations of SIP and electrification in WRF, and designed the numerical experiments. SH, JY, and QC performed the analysis and prepared the manuscript. QZ and FG contribute to the model evaluation. QZ and FG provided input on the method and analysis. All authors provided significant feedback on the manuscript.

535　**Competing interests**

The contact author has declared that none of the authors has any competing interests.

References

Baker, M. B., Christian, H. J., and Latham, J.: A computational study of the relationships linking lightning frequency and other
545　thundercloud parameters, Q.J Royal Met. Soc., 121, 1525–1548, https://doi.org/10.1002/qj.49712152703, 1995.

Bigg, E. K.: The formation of atmospheric ice crystals by the freezing of droplets, Q.J Royal Met. Soc., 79, 510–519, https://doi.org/10.1002/qj.49707934207, 1953

Brooks, I. M., Saunders, C. P. R., Mitzeva, R. P., and Peck, S. L.: The effect on thunderstorm charging of the rate of rime accretion by graupel, Atmospheric Research, 43, 277–295, https://doi.org/10.1016/S0169-8095(96)00043-9, 1997.

550   Chaudhuri, S. and Middey, A.: Effect of meteorological parameters and environmental pollution on thunderstorm and lightning activity over an urban metropolis of India, Urban Climate, 3, 67–75, https://doi.org/10.1016/j.uclim.2013.03.003, 2013.

Deshmukh, A., Phillips, V. T. J., Bansemer, A., Patade, S., and Waman, D.: New Empirical Formulation for the Sublimational Breakup of Graupel and Dendritic Snow, Journal of the Atmospheric Sciences, 79, 317–336, https://doi.org/10.1175/JAS-D-20-0275.1, 2022.

555   Fierro, A. O. and Mansell, E. R.: Electrification and Lightning in Idealized Simulations of a Hurricane-Like Vortex Subject to Wind Shear and Sea Surface Temperature Cooling, Journal of the Atmospheric Sciences, 74, 2023–2041, https://doi.org/10.1175/JAS-D-16-0270.1, 2017.

Fierro, A. O. and Reisner, J. M.: High-Resolution Simulation of the Electrification and Lightning of Hurricane Rita during the Period of Rapid Intensification, Journal of the Atmospheric Sciences, 68, 477–494, https://doi.org/10.1175/2010JAS3659.1, 560   2011.

Fierro, A. O., Mansell, E. R., MacGorman, D. R., and Ziegler, C. L.: The Implementation of an Explicit Charging and Discharge Lightning Scheme within the WRF-ARW Model: Benchmark Simulations of a Continental Squall Line, a Tropical Cyclone, and a Winter Storm, Monthly Weather Review, 141, 2390–2415, https://doi.org/10.1175/MWR-D-12-00278.1, 2013.

Hallett, J. and Mossop, S. C.: Production of secondary ice particles during the riming process, Nature, 249, 26–28, 565   https://doi.org/10.1038/249026a0, 1974.

Hallett, J. and Saunders, C. P. R.: Charge Separation Associated with Secondary Ice Crystal Production, J. Atmos. Sci., 36, 2230–2235, https://doi.org/10.1175/1520-0469(1979)036<2230:CSAWSI>2.0.CO;2, 1979.

Hong, S.-Y., Noh, Y., and Dudhia, J.: A New Vertical Diffusion Package with an Explicit Treatment of Entrainment Processes, Monthly Weather Review, 134, 2318–2341, https://doi.org/10.1175/MWR3199.1, 2006.

570   Huang, S., Jing, X., Yang, J., Zhang, Q., Guo, F., Wang, Z., and Chen, B.: Modeling the Impact of Secondary Ice Production on the Charge Structure of a Mesoscale Convective System, JGR Atmospheres, 129, e2023JD039303, https://doi.org/10.1029/2023JD039303, 2024.

Huang, S.: Modelling the impact of secondary ice production on the charge structure of a mesoscale convective system. [Dataset]. Zenodo. https://doi.org/10.5281/zenodo.7968790, 2023.

575   Jiménez, P. A., Dudhia, J., González-Rouco, J. F., Navarro, J., Montávez, J. P., and García-Bustamante, E.: A Revised Scheme for the WRF Surface Layer Formulation, Monthly Weather Review, 140, 898–918, https://doi.org/10.1175/MWR-D-11-00056.1, 2012.

Khain, Leung, L. R., Lynn, B., and Ghan, S.: Effects of aerosols on the dynamics and microphysics of squall lines simulated by spectral bin and bulk parameterization schemes, J. Geophys. Res., 114, D22203, https://doi.org/10.1029/2009JD011902, 580   2009.

Khain, A., Ovtchinnikov, M., Pinsky, M., Pokrovsky, A., and Krugliak, H.: Notes on the state-of-the-art numerical modeling of cloud microphysics, Atmospheric Research, 55, 159–224, https://doi.org/10.1016/S0169-8095(00)00064-8, 2000.

Khain, A., Cohen, N., Lynn, B., and Pokrovsky, A.: Possible Aerosol Effects on Lightning Activity and Structure of Hurricanes, Journal of the Atmospheric Sciences, 65, 3652–3677, https://doi.org/10.1175/2008JAS2678.1, 2008.

585 Khain, A. P., Beheng, K. D., Heymsfield, A., Korolev, A., Krichak, S. O., Levin, Z., Pinsky, M., Phillips, V., Prabhakaran, T., Teller, A., van den Heever, S. C., and Yano, J.-I.: Representation of microphysical processes in cloud-resolving models: Spectral (bin) microphysics versus bulk parameterization: BIN VS BULK, Rev. Geophys., 53, 247–322, https://doi.org/10.1002/2014RG000468, 2015.

Korolev, A. and Leisner, T.: Review of experimental studies of secondary ice production, Atmos. Chem. Phys., 20, 11767–590 11797, https://doi.org/10.5194/acp-20-11767-2020, 2020.

Lighezzolo, R. A., Pereyra, R. G., and Avila, E. E.: Measurements of electric charge separated during the formation of rime by the accretion of supercooled droplets, Atmos. Chem. Phys., 10, 1661–1669, https://doi.org/10.5194/acp-10-1661-2010, 2010.

Lynn, B., Khain, A., Rosenfeld, D., and Woodley, W. L.: Effects of aerosols on precipitation from orographic clouds, J. 595 Geophys. Res., 112, 2006JD007537, https://doi.org/10.1029/2006JD007537, 2007.

Lynn, B. H., Yair, Y., Shpund, J., Levi, Y., Qie, X., and Khain, A.: Using Factor Separation to Elucidate the Respective Contributions of Desert Dust and Urban Pollution to the 4 January 2020 Tel Aviv Lightning and Flash Flood Disaster, J. Geophys. Res. Atmos., 125, https://doi.org/10.1029/2020JD033520, 2020.

Mansell, E. R. and Ziegler, C. L.: Aerosol Effects on Simulated Storm Electrification and Precipitation in a Two-Moment Bulk 600 Microphysics Model, Journal of the Atmospheric Sciences, 70, 2032–2050, https://doi.org/10.1175/JAS-D-12-0264.1, 2013.

Mansell, E. R., MacGorman, D. R., Ziegler, C. L., and Straka, J. M.: Charge structure and lightning sensitivity in a simulated multicell thunderstorm, J. Geophys. Res., 110, D12101, https://doi.org/10.1029/2004JD005287, 2005.

Meyers, M. P., DeMott, P. J., and Cotton, W. R.: New Primary Ice-Nucleation Parameterizations in an Explicit Cloud Model, J. Appl. Meteor., 31, 708–721, https://doi.org/10.1175/1520-0450(1992)031<0708:NPINPI>2.0.CO;2, 1992.

605 Mitzeva, R., Saunders, C., and Tsenova, B.: Parameterisation of non-inductive charging in thunderstorm regions free of cloud droplets, Atmospheric Research, 82, 102–111, https://doi.org/10.1016/j.atmosres.2005.12.006, 2006.

Mlawer, E. J., Taubman, S. J., Brown, P. D., Iacono, M. J., and Clough, S. A.: Radiative transfer for inhomogeneous atmospheres: RRTM, a validated correlated-k model for the longwave, J. Geophys. Res., 102, 16663–16682, https://doi.org/10.1029/97JD00237, 1997.

610 Mossop S. C. and Hallett J.: Ice Crystal Concentration in Cumulus Clouds: Influence of the Drop Spectrum, Science, 186, 632–634, https://doi.org/10.1126/science.186.4164.632, 1974.

Naccarato, K. P., Pinto, O., and Pinto, I. R. C. A.: Evidence of thermal and aerosol effects on the cloud-to-ground lightning density and polarity over large urban areas of Southeastern Brazil, Geophysical Research Letters, 30, 2003GL017496, https://doi.org/10.1029/2003GL017496, 2003.

615 Pan, Z., Mao, F., Rosenfeld, D., Zhu, Y., Zang, L., Lu, X., Thornton, J. A., Holzworth, R. H., Yin, J., Efraim, A., and Gong, W.: Coarse sea spray inhibits lightning, Nat Commun, 13, 4289, https://doi.org/10.1038/s41467-022-31714-5, 2022.

Phillips, Vaughan, T. J., Yano, Jun-Ichi, Khain, and Alexander.: Ice Multiplication by Breakup in Ice-Ice Collisions. Part I: Theoretical Formulation., Journal of the Atmospheric Sciences, 2017.

620 Phillips, V. T. J. and Patade, S.: Multiple Environmental Influences on the Lightning of Cold-Based Continental Convection. Part II: Sensitivity Tests for Its Charge Structure and Land–Ocean Contrast, Journal of the Atmospheric Sciences, 79, 263–300, https://doi.org/10.1175/JAS-D-20-0234.1, 2022.

Phillips, V. T. J., Patade, S., Gutierrez, J., and Bansemer, A.: Secondary Ice Production by Fragmentation of Freezing Drops: Formulation and Theory, Journal of the Atmospheric Sciences, 75, 3031–3070, https://doi.org/10.1175/JAS-D-17-0190.1, 2018.

625 Phillips, V. T. J., Formenton, M., Kanawade, V. P., Karlsson, L. R., Patade, S., Sun, J., Barthe, C., Pinty, J.-P., Detwiler, A. G., Lyu, W., and Tessendorf, S. A.: Multiple Environmental Influences on the Lightning of Cold-Based Continental Cumulonimbus Clouds. Part I: Description and Validation of Model, Journal of the Atmospheric Sciences, 77, 3999–4024, https://doi.org/10.1175/JAS-D-19-0200.1, 2020.

Pinto, I. R. C. A., Pinto, O., Gomes, M. A. S. S., and Ferreira, N. J.: Urban effect on the characteristics of cloud-to-
630 groundlightning over Belo Horizonte-Brazil, Ann. Geophys., 22, 697–700, https://doi.org/10.5194/angeo-22-697-2004, 2004.

Pruppacher, H. R. and Klett, J. D.: Microphysics of Clouds and Precipitation, Oxford University Press, 1997.

Qu, Y., Chen, B., Ming, J., Lynn, B. H., and Yang, M.-J.: Aerosol Impacts on the Structure, Intensity, and Precipitation of the Landfalling Typhoon Saomai (2006): Aerosol Impacts on Typhoon Saomai (2006), J. Geophys. Res. Atmos., 122, 11,825-11,842, https://doi.org/10.1002/2017JD027151, 2017.

635 Qu, Y., Khain, A., Phillips, V., Ilotoviz, E., Shpund, J., Patade, S., and Chen, B.: The Role of Ice Splintering on Microphysics of Deep Convective Clouds Forming Under Different Aerosol Conditions: Simulations Using the Model With Spectral Bin Microphysics, J. Geophys. Res. Atmos., 125, https://doi.org/10.1029/2019JD031312, 2020.

Reynolds, S. E., Brooks, M., and Gourley, M. F.: Thunderstorm charge separation, J. Meteor., 14, 426–436, 1957.

Rosenfeld, D.: TRMM observed first direct evidence of smoke from forest fires inhibiting rainfall, Geophysical Research
640 Letters, 26, 3105–3108, https://doi.org/10.1029/1999GL006066, 1999.

Rosenfeld, D.: Suppression of Rain and Snow by Urban and Industrial Air Pollution, Science, 287, 1793–1796, https://doi.org/10.1126/science.287.5459.1793, 2000.

Rosenfeld, D. and Woodley, W. L.: Deep convective clouds with sustained supercooled liquid water down to -37.5 °C, Nature, 405, 440–442, https://doi.org/10.1038/35013030, 2000.

645 Rosenfeld, D., Lohmann, U., Raga, G. B., O'Dowd, C. D., Kulmala, M., Fuzzi, S., Reissell, A., and Andreae, M. O.: Flood or Drought: How Do Aerosols Affect Precipitation?, Science, 321, 1309–1313, https://doi.org/10.1126/science.1160606, 2008.

Santachiara, G., Belosi, F., and Prodi, F.: The Mystery of Ice Crystal Multiplication in a Laboratory Experiment, Journal of the Atmospheric Sciences, 71, 89–97, https://doi.org/10.1175/JAS-D-13-0117.1, 2014.

Saunders, C. P. R. and Peck, S. L.: Laboratory studies of the influence of the rime accretion rate on charge transfer during
650 crystal/graupel collisions, J. Geophys. Res., 103, 13949–13956, https://doi.org/10.1029/97JD02644, 1998.

Saunders, C. P. R., Keith, W. D., and Mitzeva, R. P.: The effect of liquid water on thunderstorm charging, J. Geophys. Res., 96, 11007, https://doi.org/10.1029/91JD00970, 1991.

Shi, Z., Li, L., Tan, Y., Wang, H., and Li, C.: A Numerical Study of Aerosol Effects on Electrification with Different Intensity Thunderclouds, Atmosphere, 10, 508, https://doi.org/10.3390/atmos10090508, 2019.

655 Shukla, B. P., John, J., Padmakumari, B., Das, D., Thirugnanasambantham, D., and Gairola, R. M.: Did dust intrusion and lofting escalate the catastrophic widespread lightning on 16th April 2019, India?, Atmospheric Research, 266, 105933, https://doi.org/10.1016/j.atmosres.2021.105933, 2022.

Stallins, J. A., Carpenter, J., Bentley, M. L., Ashley, W. S., and Mulholland, J. A.: Weekend–weekday aerosols and geographic variability in cloud-to-ground lightning for the urban region of Atlanta, Georgia, USA, Reg Environ Change, 13, 137–151, 660 https://doi.org/10.1007/s10113-012-0327-0, 2013.

Sun, M., Li, Z., Wang, T., Mansell, E. R., Qie, X., Shan, S., Liu, D., and Cribb, M.: Understanding the Effects of Aerosols on Electrification and Lightning Polarity in an Idealized Supercell Thunderstorm via Model Emulation, JGR Atmospheres, 129, e2023JD039251, https://doi.org/10.1029/2023JD039251, 2024.

Takahashi: Riming Electrification as a Charge Generation Mechanism in Thunderstorms, J. Atmos. Sci., 35, 1536–1548, 665 https://doi.org/10.1175/1520-0469(1978)035<1536:REAACG>2.0.CO;2, 1978.

Takahashi, Nagao, Y., and Kushiyama, Y.: Possible High Ice Particle Production during Graupel–Graupel Collisions, J. Atmos. Sci., 52, 4523–4527, https://doi.org/10.1175/1520-0469(1995)052<4523:PHIPPD>2.0.CO;2, 1995.

Takahashi, T.: A Numerical Simulation of Winter Cumulus Electrification. Part I: Shallow Cloud, J. Atmos. Sci., 40, 1257– 1280, https://doi.org/10.1175/1520-0469(1983)040<1257:ANSOWC>2.0.CO;2, 1983.

670 Tan, Y. B., Shi, Z., Chen, Z. L., Peng, L., Yang, Y., Guo, X. F., and Chen, H. R.: A numerical study of aerosol effects on electrification of thunderstorms, Journal of Atmospheric and Solar-Terrestrial Physics, 154, 236–247, https://doi.org/10.1016/j.jastp.2015.11.006, 2015.

Tewari, M., Chen, F., Wang, W., Dudhia, J., LeMone, M. A., Mitchell, K., Ek, M., Gayno, G., Wegiel, J., and Cuenca, R. H.: Implementation and verification of the unified NOAH land surface model in the WRF model, 20th conference on weather 675 analysis and forecasting/16th conference on numerical weather prediction, 11–15, 2004.

Twomey, S.: The Influence of Pollution on the Shortwave Albedo of Clouds, J. Atmos. Sci., 34, 1149–1152, https://doi.org/10.1175/1520-0469(1977)034<1149:TIOPOT>2.0.CO;2, 1977.

Vardiman, L.: The Generation of Secondary Ice Particles in Clouds by Crystal–Crystal Collision, J. Atmos. Sci., 35, 2168– 2180, https://doi.org/10.1175/1520-0469(1978)035<2168:TGOSIP>2.0.CO;2, 1978.

680 Wang, Y., Wan, Q., Meng, W., Liao, F., Tan, H., and Zhang, R.: Long-term impacts of aerosols on precipitation and lightning over the Pearl River Delta megacity area in China, Atmos. Chem. Phys., 11, 12421–12436, https://doi.org/10.5194/acp-11-12421-2011, 2011.

Yang, J., Wang, Z., Heymsfield, A., and Luo, T.: Liquid-ice mass partition in tropical maritime convective clouds, J. Atmos. Sci., 73, 4959–4978, https://doi.org/10.1175/JAS-D-15-0145.1, 2016.

685   Yang, J., Wang, Z., Heymsfield, A. J., DeMott, P. J., Twohy, C. H., Suski, K. J., and Toohey, D. W.: High Ice Concentration
      Observed in Tropical Maritime Stratiform Mixed-Phase Clouds with Top Temperatures Warmer than −8 °C, Atmos. Res., 233,
      104719, https://doi.org/10.1016/j.atmosres.2019.104719, 2020.

      Yang, J., Huang, S., Yang, T., Zhang, Q., Deng, Y., and Liu, Y.: Impact of ice multiplication on the cloud electrification of a
      cold-season thunderstorm: a numerical case study, Atmos. Chem. Phys., 24, 5989–6010, https://doi.org/10.5194/acp-24-5989-
690   2024, 2024.